

19 **Abstract**

20 The state of coupling between clouds and surface or boundary-layer have been
21 investigated much more extensively for marine stratocumulus clouds than for
22 continental low clouds, partly due to more complex thermodynamic structures over land.
23 A manifestation is a lack of robust remote sensing methods to identify coupled and
24 decoupled clouds over land. Here, we have generalized the concept of coupling and
25 decoupling to low clouds over land, based on potential temperature profiles.
26 Furthermore, by using ample measurements from a lidar and a suite of surface
27 meteorological instruments at the U.S. Department of Energy's Atmospheric Radiation
28 Measurement Program's Southern Great Plains site from 1998 to 2019, we have
29 developed a method to simultaneously retrieve the planetary boundary layer (PBL)
30 height (PBLH) and coupled states under cloudy conditions during the daytime. The
31 coupled states derived from lidar show strong consistency with those derived from
32 radiosondes. Retrieving the PBLH under cloudy conditions that has been a persistent
33 problem in lidar remote sensing, is resolved in this study. Our method can lead to high-
34 quality retrievals of the PBLH under cloudy conditions, and the determination of cloud
35 coupling states. With the new method, we find that coupled clouds are sensitive to
36 changes in the PBL, with a strong diurnal cycle whereas decoupled clouds and the PBL
37 are weakly related. Since coupled and decoupled clouds have distinct features, our new
38 method offers an advanced tool to separately investigate them in climate systems.

39 1 Introduction

40 A large fraction of low clouds is driven by surface fluxes through the conduits of
41 the planetary boundary layer (PBL) over land (e.g., Betts, 2009; Ek and Holtslag, 2004;
42 Golaz et al., 2002; Teixeira and Hogan, 2002; Zheng et al., 2020; Wei et al., 2020;
43 Santanello et al., 2018). This is a coupled cloud-surface system (Cheruy et al., 2014;
44 Zheng and Rosenfeld, 2015; Wu et al., 1998). However, not all low clouds respond to
45 surface forcing. Those clouds without close interactions with the local surface are
46 considered to be in a decoupled state. Given that the PBL is, by definition, the lowest
47 atmospheric layer influenced by the underlying surface (Stull, 1988), to what degree
48 the PBL top overlaps with cloud bases becomes a good criterion to separate coupled
49 and decoupled low clouds.

50 Conventionally, the “coupled state” of a cloud-topped marine boundary layer
51 implies that the moist conserved variables are vertically well mixed within the PBL
52 (Bretherton and Wyant, 1997; Dong et al., 2015; Zheng and Li, 2019; Zheng et al.,
53 2018). However, such a definition cannot be simply applied to clouds over land since
54 the moist conserved variables typically show considerable variations due to the
55 relatively complex thermodynamics (Driedonks, 1982; Stull, 1988). The definition and
56 the determination methods of the PBL over land also widely differ from those over
57 ocean (Garratt, 1994; Vogelezang and Holtslag, 1996). The concept of coupled and
58 decoupled states is typically used to characterize marine stratocumulus clouds due to
59 their large-scale coverages (Nicholls, 1984). Since stratocumulus only constitutes a
60 relatively small portion of continental clouds (Warren et al., 1986), we attempt to extend

61 the concept of coupling and decoupling to characterize low clouds over land.

62 Following parcel theory, the lifted condensation level (LCL) has been used to
63 diagnose a coupled cloud, based on the distance between the LCL and the cloud base
64 (e.g., Dong et al., 2015; Glenn et al., 2020; Zheng and Rosenfeld, 2015; Zheng et al.,
65 2020). When potential temperature and humidity are uniformly distributed in the
66 vertical, the LCL should be consistent with the cloud base for coupled cases. However,
67 the cloud base for coupled cases can considerably differ from the LCL over land
68 because potential temperature and humidity have large variabilities in the vertical scale
69 within the PBL over land (Guo et al., 2016; Stull, 1988; Su et al., 2017a). Therefore, a
70 robust remote sensing method is still warranted to distinguish coupled and decoupled
71 clouds over land.

72 Since the PBL height (PBLH) is the maximum height directly influenced by surface
73 fluxes, we consider coupling with the PBL equivalent to coupling with the land surface.
74 Thus, we use the PBLH as a critical parameter to diagnose the coupling between clouds
75 and the land surface. The degree of coupling may thus be gauged in terms of
76 quantitative differences between the cloud base and the PBL top. Such differences can
77 be determined in a height coordinate system or in a potential temperature coordinate
78 system (Kasahara, 1974). For this purpose, ground-based lidar has great potential
79 because it can continuously track the development of the PBL (Demoz et al., 2006;
80 Hageli et al., 2000; Sawyer and Li, 2013; Su et al., 2017b) and clouds (Clothiaux et al.,
81 2000; Platt et al., 1994; Zhao et al., 2014) at high temporal and vertical resolutions.

82 By jointly using lidar measurements and meteorological data from the U.S.

83 Department of Energy’s Atmospheric Radiation Measurement (ARM) Southern Great
84 Plains (SGP) site (36.6°N, 97.48°W), we attempt to identify coupled and decoupled low
85 clouds during the daytime. Unlike previous studies that use the LCL or radiosonde (RS)
86 data to diagnose coupled clouds (e.g., Dong et al., 2015; Zheng and Rosenfeld, 2015),
87 this study provides the first lidar-based method to automatically determine the coupling
88 and decoupling of low clouds over land at a high temporal resolution.

89 The paper is organized as follows. Section 2 describes the measurements and data.
90 Section 3 describes the new methodology in terms of the definition and implementation.
91 The performance of the method is demonstrated in Section 4, and a summary is
92 presented in Section 5.

93

94 **2 Data Descriptions**

95 *2.1 Radiosonde*

96 RS launches took place at least four times per day at the ARM SGP site, usually at
97 0030, 0630, 1230, and 1830 local time (LT). Holdridge et al. (2011) provide technical
98 details about the ARM RS (<https://www.arm.gov/capabilities/instruments/sonde>). In
99 this study, we consistently use daylight saving time (Coordinated Universal Time -5 h)
100 as local time throughout the year to avoid inconsistencies between summer and winter.
101 Besides the routine measurements, there are fewer, but still considerable numbers of
102 RS data obtained at other times of the day (e.g., 0930, 1200, 1300, 1530, and 1900 LT).
103 These supplemental RS samples at other times comprise ~10% of the total number of

104 cases. RS data from 0630–1900 LT are utilized in this study. The vertical resolution of
105 RS data varies according to the rising rate of the balloon, but measurements are
106 generally taken ~10 m apart. We further vertically average the RS data to achieve a
107 vertical resolution of 5 hPa.

108 There are several methods to determine PBLH from RS-measured temperature,
109 pressure, and humidity profiles. They include, among others, the parcel method
110 (Holzworth, 1964), the gradient methods (Stull, 1988; Seidel et al., 2010), and the
111 Richardson number method (Vogelezang and Holtslag, 1996). After examining the
112 previous methods, Liu and Liang (2010) proposed a different approach to determine the
113 PBLH that is valid under different thermodynamic conditions. The robust performance
114 was demonstrated over the SGP site and in other major field campaign sites around the
115 world (Liu and Liang, 2010). Thus, we adopted this method to calculate PBLH from
116 RS data in this study. The potential temperature is corrected as the virtual potential
117 temperature, θ_v , using the water vapor mixing ratio [WVMR; $\theta_v = (1 + 0.61 \text{WVMR})$].
118 The virtual potential temperature does not include a correction for the liquid water
119 content profile, as this is challenging to measure in many conditions. Therefore, the
120 virtual potential temperature is not conserved during moist convection. Since we mainly
121 focus on the sub-cloud atmosphere, this is not a serious problem. Moreover, we use
122 scaled RS moisture profiles normalized by the total precipitable water vapor derived
123 from the microwave radiometer (<https://www.arm.gov/capabilities/vaps/lssonde>,
124 Revercomb et al., 2003).

125

126 2.2 Micropulse lidar (MPL) system

127 MPL backscatter profiles were collected at the SGP site from September 1998 to
128 July 2019 with high continuity (Campbell et al., 2002). Technical details and data
129 availability can be found at the website
130 <https://www.arm.gov/capabilities/instruments/mpl>. The backscatter profiles have a
131 vertical resolution of 30 m. MPL signals have an initial temporal resolution of 10–30 s
132 and are averaged every 10 min for this study. Due to the inherent problem of lidar
133 observations, there is a ~0.2-km near-surface “blind zone”. Following the standard
134 lidar-data processing, background subtraction, signal saturation and overlapping, after-
135 pulse and range corrections are applied to the raw MPL data (Campbell et al., 2002,
136 2003). Questionable data are excluded based on the quality-control flags.

137

138 2.3 Cloud product

139 The MPL can be used to detect cloud layers based on signal gradients (Platt et al.,
140 1994). Lidar-based methods are accurate for determining the cloud-base height (CBH)
141 but may miss information about the cloud top due to the signal saturation within an
142 optically thick cloud (Clothiaux et al., 2000). Under this condition, the cloud radar
143 provides a better estimation of the cloud-top height (CTH). In this study, we directly
144 use an existing quality-controlled cloud product, CLDTYPE/ARSCL
145 (<https://www.arm.gov/capabilities/vaps/cldtype>), which combines information from
146 the MPL, ceilometer, and cloud radar to determine the vertical boundaries of clouds
147 (Clothiaux et al., 2000; Flynn et al., 2017). For the lowest cloud base, the best

148 estimation from laser-based techniques (i.e., MPL and ceilometer) is used. The original
149 temporal resolution of the CLDTYPE/ARSCL product is 1 min, averaged to a 10-min
150 temporal resolution. To avoid averaging jumps in signal between different clouds, a
151 cloud is considered to be continuous if its base height varies less than 0.25 km between
152 two consecutive profiles.

153

154 **3 Methodology**

155 *3.1 Definition of coupled and decoupled clouds based on thermodynamics*

156 The definition of the state of cloud-surface coupling over land is a critical question.
157 For marine stratocumulus, coupled clouds are identified when the liquid water potential
158 temperature varies less than a certain threshold (i.e., 0.5 K) below the cloud base (Jones
159 et al., 2011). We try to extend the concept of coupling and decoupling to clouds over
160 land. The PBL over land is typically buoyancy driven and controlled by surface fluxes
161 during the daytime. We consider a cloud is in the coupled state when it strongly interacts
162 with the buoyancy fluxes within the PBL.

163 Figure 1 presents the idealized vertical profiles of virtual potential temperature (θ_v)
164 under the clear-sky, coupled cloud, and decoupled cloud. A superadiabatic surface layer
165 exchanges the heat fluxes between the surface and PBL. The outer layer and
166 entrainment zone are turbulently coupled with the surface, and thus, are considered as
167 the coupled regime. Meanwhile, the free atmosphere is considered as the decoupled
168 regime. Theoretically, θ_v is constant in the outer layer, and follows the wet adiabatic

169 lapse rate in the cloud layer. Although the profiles of θ_v in the real atmosphere can
170 largely differ from the idealized profiles, the relative position between the cloud layer
171 and capping inversion of entrainment zone is clear. For the coupled cases, the cloud
172 base is below the capping inversion of entrainment zone. For the decoupled cases, the
173 cloud base is above the capping inversion. Based on this feature, we can use the virtual
174 potential temperature profiles to diagnose the coupling state of low clouds.

175 We first look at several examples of profiles of θ_v and WVMR from the RS
176 (Figure 2). If the CBH is lower than the PBLH, the cloud is affected by turbulence and
177 buoyancy fluxes in the PBL, such as the cases shown in Figure 2a. Note that the PBLH
178 is not an absolute boundary limiting turbulence and buoyancy fluxes. Due to the
179 overshooting of rising air parcels, we use a range to screen the condition of coupled
180 clouds. As shown in Figure 2b, even when the CBH is slightly above the PBLH,
181 WVMR and θ_v are still relatively consistent between the cloud layer and the PBL and
182 show large step signals at the cloud top.

183 Figure 2c-d shows a clear inversion layer between the cloud base and the PBL top,
184 and the difference in θ_v between the CBH and the PBLH ($\Delta\theta_v$) is relatively large.
185 Such a notable inversion layer prevents the buoyancy fluxes within the PBL from
186 reaching the cloud base, leading to the decoupling between the cloud and the PBL.
187 Overall, whether there is a clear inversion between the cloud base and the PBL top is
188 the key factor in determining coupling and decoupling. In this aspect, $\Delta\theta_v$ is the key
189 factor. In Figure 2, $\Delta\theta_v$ for coupled cases (a-c) is -0.32 K and 0.31 K, respectively,
190 and $\Delta\theta_v$ for decoupled cases (d-e) is 1.47 K and 5.0 K, respectively.

191 Therefore, instead of giving a height range to limit the differences between CBH
192 and PBLH, we consider using the differences in θ_v between CBH and PBLH to
193 determine the threshold for distinguishing coupled and decoupled clouds. For
194 convenience, we use $\Delta\theta_v$ to refer to the difference in θ_v between the CBH and the
195 PBLH ($\Delta\theta_v = \theta_v^{\text{CBH}} - \theta_v^{\text{PBLH}}$). For decoupled cases, the cloud base is above the
196 capping inversion of entrainment zone. There is a notable inversion in θ_v between
197 PBL top and decoupled cloud base. Thus, we identify the cases satisfying $\Delta\theta_v > \delta_s$ as
198 being in a decoupled state. Correspondingly, we identify the cases satisfying $\Delta\theta_v < \delta_s$
199 as being in a coupled state. We set the range of CBH to between 0 and 4 km and
200 excluded cases of deep convection (i.e., $\text{CBH} < 4 \text{ km}$ and $\text{CTH} > 6.5 \text{ km}$).

201 As the basic framework of PBL, the slab model assumes that θ_v is constant within
202 the PBL (Wallace and Hobbs, 2006). Under this assumption, δ_s can be set as 0.
203 However, there are certain variations in θ_v within the PBL, which can cause inversions
204 with relatively small magnitudes between the cloud base and PBL top. Figure 3a
205 presents the inversion strength in θ_v within PBL during the daytime. Specifically,
206 inversions represent the layers with continuously increased structures of θ_v . For an
207 inversion layer, the inversion strength is calculated as the differences in θ_v between the
208 top and bottom of the layer. The inversions near surface or across the PBL top are
209 excluded. Besides the capping inversion and surface inversion, the inversion strength
210 within PBL is typically below 1K. Therefore, we set δ_s as 1 K, which is the same as
211 the criterion for determining stable or convective conditions (Liu and Liang, 2010).
212 Furthermore, we demonstrate the probability density function (PDF) of $\Delta\theta_v$ for the

213 low cloud cases. Coupled and decoupled clouds are classified by the threshold of δ_s
214 (1 K). Through the development of PBL, boundary layer clouds frequently occur in the
215 entrainment zone, and form a coupled cloud-PBL system. For such coupled systems,
216 θ_v at cloud top and PBL top is highly consistent for the majority of cases. Thus, the
217 PDF of $\Delta\theta_v$ shows significantly high values for the range of -2 K to 0.5 K in the
218 coupled regime. Meanwhile, the PDF of $\Delta\theta_v$ is evenly distributed in the decoupled
219 regime. Since we only analyze low clouds, the PDF of $\Delta\theta_v$ slowly decrease when $\Delta\theta_v$
220 is above 10 K.

221 Based on the variations in θ_v within PBL, we set δ_s as 1 K. However, it should
222 note that it is not an absolute value. A similar threshold of 0.5 K has been used for
223 marine stratocumulus (Jones et al., 2011; Dong et al., 2015). Comparing to the marine
224 condition, θ_v show greater variabilities over land. Hence, the threshold is
225 correspondingly larger. On the other hand, since the threshold of 1 K is in the low PDF
226 regime (Figure 3b), the small changes in this value would not notably affect the
227 identifications. Specifically, a 0.1 K difference in δ_s will lead to a 0.5% difference in
228 the identification of coupled cloud.

229 Same to the previous studies (Jones et al., 2010; Dong et al., 2015; Zheng and
230 Rosenfeld, 2015), we identified the coupled clouds as the thermodynamics coupling
231 between surface and cloud base. However, it is an open question whether the entire
232 cloud layer is coupled for coupled cases. It depends on whether the liquid water
233 potential temperature is conserved within the cloud layer, which represents a moisture
234 adiabatic process. This issue is closely related to the cloud types. In the cloud

235 parameterizations, the entire stratocumulus layer is considered to be well-mixed,
236 while the cumulus-capped layer is usually partially mixed (Lock, 2000). For
237 stratocumulus clouds, the entire cloud layer and PBL are typically fully coupled with
238 surface, when the cloud base is coupled with surface. For the cumulus-capped PBL, the
239 entire cloud layer may not be completely coupled, despite the coupling between cloud
240 base and surface. The well-established parameterizations are supported by many
241 observational studies (e.g., Betts, 1986; Storer et al., 2015; Berkes et al., 2016, de Roode
242 and Wang, 2006; Ott et al., 2009).

243

244 *3.2 Lidar-based method to identify coupled and decoupled clouds*

245 *3.2.1 Method description*

246 Given the rapid change in clouds over land, RS observations have limitations when
247 it comes to tracking cloud development due to the coarse temporal resolution and
248 drifting of the balloon. We thus further developed a lidar-based method to identify the
249 coupled states of clouds based on our new algorithm for retrieving the PBLH that can
250 better track the diurnal variations in PBLH than conventional lidar-based approaches
251 (Su et al., 2020). We adapted this algorithm for retrieving the PBLH and developed a
252 new scheme to deal with cloudy conditions. Following the original method (Su et al.
253 2020), the rainy cases are eliminated in the quality control process. The principles
254 behind the PBLH algorithm are stated next for completeness.

255 Our new PBLH algorithm can retrieve the PBL variability from the MPL under

256 Different Thermo-Dynamic Stability (thus named the DTDS algorithm) conditions,
257 taking into account the vertical coherence and temporal continuity of the PBLH. First,
258 we identify the local maximum positions (LMPs; range: 0.25–4 km) in profiles of the
259 wavelet covariance transform function derived from lidar backscatter (Brooks, 2003).
260 These LMPs are the potential positions of the PBLH. We can use the PBLH derived
261 from morning RS soundings as the starting point. Without morning RS soundings, the
262 algorithm can still work well, with the lowest LMPs selected as the starting point, which
263 reduces by 0.02–0.05 the correlation coefficient between MPL-derived and RS-derived
264 PBLHs (Su et al., 2020).

265 To ensure good continuity, we select the closest LMP to the earlier position of the
266 PBLH. Different stages of PBL development are considered. DTDS-derived PBLHs
267 likely increase during the growth stage and decrease during the decaying stage, but the
268 algorithm is also able to identify decreases during the growth stage or increases during
269 the decaying stage based on the selection scheme described by Su et al. (2020). There
270 are multiple step signals in the backscatter profiles when complex aerosol structures
271 (e.g., the residual layer) are present, leading to multiple LMPs. Based on temporal
272 continuity, we select the appropriate LMP as the position of the PBL top. However,
273 PBLH retrievals still suffer from relatively low accuracies under stable conditions
274 because of the weak vertical mixing and residual layer.

275 Clouds induce strong step signals in the lidar backscatter, further considerably
276 affecting PBLH retrievals. Su et al. (2020) only considered cases where the low cloud
277 top coincided with the previous PBL top, excluding other low-cloud cases (> 60% of

278 all low-cloud cases). Here, we specifically consider coupled and decoupled states of
279 low clouds. Due to the MPL's ~0.2-km blind zone, we only analyze the PBLH and CBH
280 above 0.2 km. Figure 4 presents the flow chart describing the updated DTDS algorithm.
281 In particular, we jointly use PBL development and the LCL to diagnose the states of
282 coupling or decoupling. In ideal situations, LCL, PBLH, and CBH are highly consistent
283 with each other for coupled clouds. But for real conditions, we only require that either
284 the LCL or the PBLH coincides with the CBH for identifying coupled cases, with
285 another parameter serving as an additional constraint. Specifically, a coupled cloud
286 needs to occur within a certain range of LCL and the previous position of the PBL top.

287 For the DTDS algorithm, five empirical parameters are used, including A_1 , A_2 ,
288 A_3 , A_4 , A_5 . As listed in the Table 1, $A_1 - A_5$ are set as 0.7, 0.2, 0.15, 1.35, and 1.1,
289 respectively. A cloud at time i is identified as being in the coupled state if the CBH is
290 less than $[H(i - 1) + 0.2 \text{ km } (A_2)]$ and $[LCL + 0.7 \text{ km } (A_1)]$. This step moves
291 39.5% of low cloud cases to the category of decoupled clouds. A cloud is also
292 considered to be in a coupled state if the CBH is coincident with the LCL within 0.15
293 km (A_3), and the CBH is less than $[H(i - 1) + 0.7 \text{ km } (A_1)]$, where $H(i - 1)$
294 represents the PBLH at time $(i - 1)$. This step further moves 17.8% of the remaining
295 cases to the category of decoupled clouds.

296 The LCL is calculated from surface meteorological data (relative humidity,
297 temperature, pressure) at the SGP site based on an exact expression (Romps, 2017).
298 Specifically, Romps. (2017) proposed an exact, explicit, analytic expression for LCL as
299 a function of surface meteorology. Compared to the previous approximate expressions,

300 some of which may have an uncertainty in the order of hundreds of meters, the Romps
301 expression can be considered as the precise value. The uncertainty of empirical vapor
302 pressure data may lead to a bias of ~5-m (Romps, 2017), which may be neglected in the
303 analyses.

304 After determining the coupling or decoupling state of a cloud, we retrieve $H(i)$
305 (i.e., PBLH at time i) based on the cloud state. For decoupled cases, we use the same
306 strategy for a clear sky to retrieve the PBLH. Based on the selection scheme in the
307 DTDS algorithm, the LMP below the CBH is selected as $H(i)$. For coupled cases, we
308 jointly use CBH and CTH to determine PBLH. During the warm season, active cumulus
309 often occurs in the upper part of the PBL with strong surface heating, so the CBH can
310 be generally regarded as the PBLH (Stull, 1988; Wallace and Hobbs, 2006). Under this
311 condition, the CBH coincides with the previous PBL top. Therefore, if $[CTH \geq$
312 $PBLH_{30min} + 0.2 \text{ km } (A_2)]$, we set $H(i) = A_5 CBH$, where $PBLH_{30min}$ is the
313 average value of the PBLH within 30 min of the prior time i . Hence, A_5 would be a
314 critical parameter for the PBLH estimation. On the other hand, if $[CTH <$
315 $PBLH_{30min} + 0.2 \text{ km } (A_2)]$, we set $H(i)$ equal to the minimum between CTH and
316 the product $A_4 * CBH$. This step is designed for thin clouds or some stratiform clouds.
317 In particular, $A_5 * CBH$ can be notably larger than the CTH for a thin cloud. Under this
318 situation, we tend to use CTH to denote the PBL top. This step has little impact on the
319 detection of surface-cloud coupling, but can assure that the CTH of the coupled cloud
320 is always higher than the retrieved PBLH to fit the real situation.

321 After retrieving $H(i)$, we consider that the cloud above the PBLH is still coupled

322 if $[CBH < H(i) + 0.2 \text{ km } (A_2)]$. Moreover, we added an upper limit for all PBLH
323 retrievals. If $[H(i) > LCL + 0.7 \text{ km } (A_1)]$, we adjust $H(i)$ as the maximum LMP
324 below the LCL. The new DTDS method combines lidar measurements and surface
325 meteorological observations and can simultaneously retrieve the PBLH and cloud states.

326

327 *3.2.2 Selection of empirical parameters*

328 The states of coupling and decoupling are diagnostic parameters rather than explicit
329 expressions. Similar to the other methods for retrieving PBLH (e.g., Brooks, 2003; Liu
330 and Liang, 2010), multiple empirical parameters are used to determine PBLH. Here we
331 discuss the selection of empirical parameters in the algorithm.

332 Note that we used the CTH and $A_4 * CBH$ as the upper limits for PBLH retrievals in
333 the DTDS algorithm. For coupled cases, these two limits are generally close to or above
334 the position of the PBL top. Only 2% (3%) of total cases meet the condition that the
335 RS-derived PBLH is 0.25 km higher than the CTH ($A_4 * CBH$). Section 4 presents the
336 detailed relationships between CBH, CTH, and PBLH. In the DTDS method, CTH
337 serves as the upper limit for PBLH under the condition of coupled shallow cumulus.

338 Similar to previous studies, we can also use the LCL as the standard to identify
339 coupled clouds (Dong et al., 2015; Zheng and Rosenfeld, 2015). We assume a cloud is
340 coupled if $|CBH - LCL| < \Delta h$. By using ~ 7500 RS profiles, the cloud coupling state
341 derived from the virtual potential temperature method (Section 3.1) is considered as the
342 ground truth for evaluation. Figure 5a shows the commission errors and omission errors

343 for different criteria. Here, the commission error is calculated as the percentage of
344 decoupled clouds misidentified as coupled clouds. The commission error can also be
345 called a “false positive”, as the former is a common term for describing the nature of
346 an error in identification. The omission error is calculated as the percentage of coupled
347 clouds that have not been identified under this criterion. By using the LCL, we can
348 obtain a relatively low commission error if the criterion is less than 0.15 km and a
349 relatively low omission error if the criterion is greater than 0.7 km. Thus, we set A_1
350 and A_3 as 0.7 and 0.15 in the DTDS method to exclude and to select cases of coupled
351 clouds. We can also use the RS-derived PBLH as the criterion (Figure 5b).

352 Despite the coarse temporal resolution, the RS-derived PBLH can be a good
353 criterion to use to distinguish between coupling and decoupling. If we consider a
354 coupled cloud as a cloud where ($CBH < RS\text{-derived PBLH} + 0.2 \text{ km}$), both commission
355 and omission errors are $\sim 5\%$. Therefore, we primarily use [$PBLH + 0.2 \text{ km}$ (A_2)] in the
356 DTDS method to identify coupled and decoupled regimes. As cloud can considerably
357 affect with lidar backscattering and generate large signal variations, we jointly use lidar
358 backscattering, the previous position of PBL top, and LCL to determine the surface-
359 cloud coupling and PBLH. In particular, the LCL constraint in the algorithm notably
360 reduces the absolute biases in PBLH retrievals under cloudy conditions by 9.3%.

361 Moreover, we test the sensitivity of selecting these empirical parameters. Figure 6
362 presents the commission errors and omission errors in the identifications of coupled
363 clouds for selecting different values of empirical parameters. Among these parameters,
364 A_2 is the critical one, which would notably affect the identification results. In general,

365 A_2 determine the maximum differences between PBLH and CBH for coupled cases. If
366 $[CBH-PBLH > A_2]$, we consider the cloud is under the decoupled state. Thus, the
367 identification method is quite sensitive to A_2 . Selecting a low value of A_2 would
368 neglect many coupled cases, which leads to a high omission error. Meanwhile, selecting
369 a high value of A_2 would misclassify many coupled cases, which leads to a high
370 commission error. After a trail and error, A_2 is set as 0.2 km to balance the omission
371 and commission errors. The selections for other parameters are not sensitive for the
372 coupled cloud identifications. We can choose them from a reasonable range.

373 As a by-product of this method, we also pay attentions to the PBLH retrievals under
374 cloudy conditions. Figure 7 presents the mean absolute biases and correlation
375 coefficients between PBLH derived from lidar and radiosonde for selecting different
376 values of empirical parameters. To match the scope of this study, we only analyze the
377 low cloud conditions. For retrieving PBLH under cloudy conditions, A_2 is the critical
378 parameter. The variations in correlation coefficients under different values of empirical
379 parameters are small with a range of 0.81-0.82. However, the absolute biases can
380 considerably differ under different values of A_5 . In general, A_5 represents the ratio
381 between CBH and PBLH under coupled conditions. If A_5 is above 1.1, PBLH
382 retrievals under cloudy conditions are overestimated. We set A_5 as 1.1 to achieve a
383 relatively low bias and a relatively high correlation coefficient at the same time. For
384 other parameters, the selections from reasonable ranges would not notably affect the
385 PBLH retrievals.

386 In short, selections of these empirical parameters are based on the overall

387 relationship between cloud and PBL under the coupled and decoupled states. In our
388 method, the selection of A_2 is critical for the identifications of coupled clouds, while
389 the selection of A_5 is critical for the PBLH retrievals under cloudy conditions. The
390 selections of other parameters are not sensitive.

391

392 **4 Results**

393 Figure 8 illustrates four examples of PBLH retrievals and cloud states derived from
394 the DTDS algorithm for 27 October 2011, 31 July 2002, 19 March 2000, and 1 May
395 2012. Figure 8a depicts coupled shallow cumulus occurring at noontime at the PBL top.
396 With a weak surface flux of $\sim 200 \text{ W m}^{-2}$, this shallow cumulus cloud appeared for less
397 than an hour. Figure 8b shows a developed coupled cumulus cloud. With a strong
398 surface flux of $\sim 500 \text{ W m}^{-2}$, this coupled cloud continuously developed during the
399 daytime. Figure 8c presents the case of a daylong coupled cloud. After the passage of a
400 frontal system that day, stratocumulus occurred during the morning with a cloud
401 thickness of 0.5 km. Through the development of the PBL, the thick stratocumulus
402 cloud was broken up by the strong turbulences, transforming into shallow cumulus
403 clouds. Figure 8d shows the case of an active coupled cloud, which is generally
404 associated with a large amount of convective available potential energy. Even though
405 coupled clouds can differ in appearance and variability throughout the day, the common
406 feature is the coherent variation between the cloud base and the PBL top. The LCL is a
407 relevant parameter and can differ from the PBLH and the CBH for some coupled cases
408 (e.g., Figure 8b-c).

409 The identification accuracy, or disparity between different methods, are evaluated
410 in terms of the selected criteria, for which the identification method based on $\Delta\theta_v$ is
411 regarded as the “truth”, as described in Section 3.1. Hereafter, all results are analyzed
412 for the period of 1000–1900 LT, so early-morning data are not used. The commission
413 error is 10.1%, and the omission error is 6.8% for the DTDS method. Note that lidar-
414 based PBLH methods generally suffer from relatively low accuracy under stable
415 atmospheric conditions. Following Liu and Liang (2010), we identified stable PBLs
416 from RS measurements. Since coupled clouds are driven by relatively strong buoyancy
417 fluxes, only 1% of total cases of coupled clouds occurred under stable PBL conditions
418 during the study period (0700–1900 LT). Therefore, the relatively low accuracy for
419 stable PBLs is not a major problem in this study.

420 Figure 5 also compares the accuracy between the DTDS and LCL methods. Based
421 on the LCL alone, we cannot choose an appropriate criterion to achieve a lower
422 commission error and omission error simultaneously. Thus, we do not use the LCL as
423 the single standard to detect the coupling and decoupling of low clouds in our study. As
424 diagnostic parameters, different methods inevitably produce different results regarding
425 coupling and decoupling. Although we consider the method based on $\Delta\theta_v$ as the
426 standard, it still suffers from uncertainties arising from balloon drifting. From this
427 perspective, it is hard to conclude which method is the best. Since it determines the
428 PBLH based on aerosol backscattering, the lidar-based method may be more
429 representative of the coupling between a cloud and the aerosol layer near the surface
430 when clear skies occur, at least during a short window of time.

431 Figure 9a-b presents the occurrence frequencies of the CBH and the CTH at
432 different heights. Despite the same variation ranges, clouds are mostly coupled if the
433 CBH is lower than 1 km, while decoupled clouds dominate if the CBH is higher than 3
434 km. Figure 9c-d shows the changes in the coupled fraction (ratio of coupled cases to
435 total cases) with different CBHs and CTHs. The coupled fraction is about 90% if the
436 CBH is lower than 1 km and decreases to 2% for CBHs above 3 km. Although the CBHs
437 for coupled cases are generally less than 3 km, CTHs for coupled cases can be much
438 higher. Coupled clouds still account for around 10% of the cases with CTHs above 6
439 km.

440 Figure 10 shows scatter plots between CBH, CTH, PBLH, and LCL for coupled
441 and decoupled clouds. For coupled clouds, there is a generally strong correlation
442 between CBH, LCL, and PBLH, contrary to the weak relationships of decoupled cases.
443 The relationship between CTH and RS-derived PBLH is complicated. For shallow
444 cumulus clouds, their tops can be considered as PBL tops for the coupled state, while
445 the cloud top is considerably above the position of the PBL top for active cumulus
446 clouds. We also note that the accuracy of CTH retrievals is generally lower than the
447 accuracy of CBH retrievals (Clothiaux et al., 2000). As CTH is not a criterion for cloud
448 coupling, the accuracy of CTH would not affect the identification of coupled cloud, but
449 may affect the PBLH retrievals for the coupled cloud cases. Meanwhile, despite the
450 laser-based detection of CBH is considered as the standard method (Platt et al., 1994;
451 Clothiaux et al., 2000; Lim et al., 2019), the CBH retrievals from ceilometer or lidar
452 still bear some uncertainties, which can potentially lead to a mean bias of 0.1km (Silber

453 et al., 2018; Cromwell et al., 2019). In our method, a systematic increase of 0.1 km in
454 the CBH can lead to an increase of 2.1% in omission errors and a decrease of 1% in
455 commission errors.

456 After identifying the coupling state of clouds, it is feasible to retrieve the PBLH
457 under cloudy conditions. In particular, the DTDS-derived PBLH needs to resort to the
458 cloud position for coupled cloud cases. For decoupled cloud cases, on the other hand,
459 the PBLH below clouds is sought to avoid cloud interference. For coupled clouds,
460 DTDS-derived PBLHs show a strong correlation with RS-derived PBLHs with a
461 correlation coefficient (R) of ~ 0.9 (Figure 10d). For decoupled cases, the correlation
462 between DTDS-derived PBLHs and RS-derived PBLHs is generally good ($R = 0.73$)
463 but worse than the correlation for coupled cases (Figure 10h). As pointed out in previous
464 studies (Chu et al., 2019; Hageli et al., 2000; Lewis et al., 2013; Su et al., 2017b), it has
465 been a persistent problem to retrieve the PBLH under cloudy conditions since the strong
466 backscattering and step signals from cloud interference would be excluded to avoid
467 interfering with the retrievals. The PBLH determined by our method under a cloudy
468 condition is much more reasonable. Moreover, due to the different definitions of the
469 PBLH and aerosol stratification within the PBL, there are always considerable
470 differences between lidar- and RS-derived PBLHs, which cannot be eliminated by a
471 specific algorithm (Chu et al., 2019; Su et al., 2020).

472

473 **5 Summary**

474 In this study, we proposed a novel method for distinguishing between coupled and

475 decoupled low clouds over land. Based on the understanding of PBL processes and
476 quantitative analyses, we developed a lidar-based method (DTDS) to identify the
477 coupling state of low clouds over the SGP site. In practice, we identified a coupled
478 cloud when the position of the cloud base was generally close to or lower than the
479 previous position of the PBL top, with the LCL serving as an additional restriction.
480 Compared to using the LCL alone, the coupled states identified by the DTDS method
481 show better consistency with the results derived from radiosondes, with about 10%
482 differences between the lidar-based retrievals and radiosonde results.

483 Not only coupled state, also retrieved by the method is the PBLH under cloudy
484 conditions. A long-lasting problem with lidar-retrieval of PBLH is either incapability
485 of retrieval or large uncertainties induced by the occurrence of low clouds (e.g., Chu et
486 al., 2019; Hageli et al., 2000; Lewis et al., 2013), we address this issue by separately
487 considering the coupled and decoupled of low clouds. Specifically, in coupled
488 conditions, the position of the coupled cloud serves as a good reference for identifying
489 the PBLH. In decoupled conditions, the large backscatter and step signals from clouds
490 would be excluded to avoid interfering with the retrievals. With our method, cloudy
491 conditions are well handled.

492 With the new method, we study the difference of cloud-PBL interactions in coupled
493 and decoupled conditions. In contrast to the sensitive responses of coupled clouds to
494 changes in the PBLH and buoyancy, the decoupled clouds and the PBLH are weakly
495 related. Due to their different relationships with the PBL, a robust distinguishment
496 between the coupled and decoupled low clouds is critical for further investigating the

497 coupled land-atmosphere system and aerosol-cloud interactions. Our methodology
498 paves a solid ground for such pursuits.

499

500 *Data availability.* All these datasets are publicly available at the ARM archive
501 https://adc.arm.gov/discovery/#/results/site_code::sgp. The products developed in this
502 study, i.e., cloud states and the PBLH, are currently available upon request from the
503 lead author (tianning@umd.edu) and are expected to be added to the ARM archive in
504 the near future.

505

506 *Author contribution.* T.S., Y.Z., and Z.L. conceptualized this study. T.S. carried out the
507 analysis, with comments from other co-authors. T.S., Y.Z., and Z.L. interpreted the data
508 and wrote the manuscript.

509

510 *Competing interests.* The authors declare that they have no conflict of interest.

511

512 *Acknowledgements.* This work was supported by grants from the U.S. Department of
513 Energy (DE-SC0018996), the National Science Foundation (AGS1837811), and NASA
514 (NNX16AN61G). We acknowledge the provision of radiosonde, MPL data, surface
515 meteorological data, and cloud products by the U.S. Department of Energy's ARM
516 program. We thank the two anonymous reviewers for their comments.

517

518 **References**

519 Berkes, F., Hoor, P., Bozem, H., Kunkel, D., Sprenger, M. and Henne, S. (2016).

520 Airborne observation of mixing across the entrainment zone during PARADE 2011.

521 *Atmospheric Chemistry and Physics*, 16(10), pp.6011-6025.

522 Betts, A.K. (2009). Land-surface-atmosphere coupling in observations and models.

523 *Journal of Advances in Modeling Earth Systems*, 1(3).

524 <https://doi.org/10.3894/JAMES.2009.1.4>

525 Bretherton, C. S., and Wyant, M. C. (1997). Moisture transport, lower-tropospheric

526 stability, and decoupling of cloud-topped boundary layers. *Journal of the*

527 *Atmospheric Sciences*, 54(1), 148–167. [https://doi.org/10.1175/1520-](https://doi.org/10.1175/1520-0469(1997)054<0148:MTL TSA>2.0.CO;2)

528 [0469\(1997\)054<0148:MTL TSA>2.0.CO;2](https://doi.org/10.1175/1520-0469(1997)054<0148:MTL TSA>2.0.CO;2)

529 Brooks, I. M. (2003). Finding boundary layer top: application of a wavelet covariance

530 transform to lidar backscatter profiles. *Journal of Atmospheric and Oceanic*

531 *Technology*, 20, 1092–1105. [https://doi.org/10.1175/1520-](https://doi.org/10.1175/1520-0426(2003)020<1092:FBLT AO>2.0.CO;2)

532 [0426\(2003\)020<1092:FBLT AO>2.0.CO;2](https://doi.org/10.1175/1520-0426(2003)020<1092:FBLT AO>2.0.CO;2)

533 Campbell, J. R., Hlavka, D. L., Welton, E. J., Flynn, C. J., Turner, D. D., Spinhirne, J.

534 D., ... Hwang, I. H. (2002). Full-time, eye-safe cloud and aerosol lidar

535 observation at atmospheric radiation measurement program sites: instruments and

536 data processing. *Journal of Atmospheric and Oceanic Technology*, 19(4), 431–442.

537 [https://doi.org/10.1175/1520-0426\(2002\)019<0431:FTESCA>2.0.CO;2](https://doi.org/10.1175/1520-0426(2002)019<0431:FTESCA>2.0.CO;2)

538 Campbell, J.R., Welton, E.J., Spinhirne, J.D., Ji, Q., Tsay, S.C., Piketh, S.J., Barenbrug,
539 M. and Holben, B.N., 2003. Micropulse lidar observations of tropospheric aerosols
540 over northeastern South Africa during the ARREX and SAFARI 2000 dry season
541 experiments. *Journal of Geophysical Research: Atmospheres*, 108(D13).

542 Cheruy, F., Dufresne, J. L., Hourdin, F., and Ducharne, A. (2014). Role of clouds and
543 land-atmosphere coupling in midlatitude continental summer warm biases and
544 climate change amplification in CMIP5 simulations. *Geophysical Research Letters*,
545 41(18), 6493–6500. <https://doi.org/10.1002/2014GL061145>

546 Chu, Y., Li, J., Li, C., Tan, W., Su, T., and Li, J. (2019). Seasonal and diurnal variability
547 of planetary boundary layer height in Beijing: intercomparison between MPL and
548 WRF results. *Atmospheric Research*, 227, 1–13.
549 <https://doi.org/10.1016/j.atmosres.2019.04.017>

550 Clothiaux, E. E., Ackerman, T. P., Mace, G. G., Moran, K. P., Marchand, R. T., Miller,
551 M. A., and Martner, B. E. (2000). Objective determination of cloud heights and
552 radar reflectivities using a combination of active remote sensors at the ARM CART
553 sites. *Journal of Applied Meteorology*, 39(5), 645–665.
554 [https://doi.org/10.1175/1520-0450\(2000\)039<0645:ODOCHA>2.0.CO;2](https://doi.org/10.1175/1520-0450(2000)039<0645:ODOCHA>2.0.CO;2)

555 Cromwell, E., and Flynn, D. (2019). Lidar cloud detection with fully convolutional
556 networks. In 2019 IEEE Winter Conference on Applications of Computer Vision
557 (WACV) (pp. 619-627). IEEE.

558 de Roode, S.R. and Wang, Q. (2007). Do stratocumulus clouds detrain? FIRE I data

559 revisited. *Boundary-layer meteorology*, 122(2), pp.479-491.

560 Demoz, B., Flamant, C., Weckwerth, T., Whiteman, D., Evans, K., Fabry, F., and
561 Schwemmer, G. (2006). The dryline on 22 May 2002 during IHOP_2002:
562 convective-scale measurements at the profiling site. *Monthly Weather Review*,
563 134(1), 294–310. <https://doi.org/10.1175/MWR3054.1>

564 Dong, X., Schwantes, A. C., Xi, B., and Wu, P. (2015). Investigation of the marine
565 boundary layer cloud and CCN properties under coupled and decoupled conditions
566 over the Azores. *Journal of Geophysical Research: Atmospheres*, 120, 6179–6191.
567 <https://doi.org/10.1002/2014JD022939>

568 Driedonks, A. G. M. (1982). Models and observations of the growth of the atmospheric
569 boundary layer. *Boundary-Layer Meteorology*, 23(3), 283–306.
570 <https://doi.org/10.1007/BF00121117>

571 Ek, M. B., and Holtslag, A. A. M. (2004). Influence of soil moisture on boundary layer
572 cloud development. *Journal of Hydrometeorology*, 5(1), 86–99.
573 [https://doi.org/10.1175/1525-7541\(2004\)005<0086:IOSMOB>2.0.CO;2](https://doi.org/10.1175/1525-7541(2004)005<0086:IOSMOB>2.0.CO;2)

574 Flynn, D., Shi, Y., Lim, K., and Riihimaki, L. (2017). Cloud Type Classification
575 (cldtype) Value-Added Product. Ed. by Robert Stafford, ARM Research Facility.
576 DOE/SC-ARM-TR-200.

577 Garratt, J. R. (1994). Review: the atmospheric boundary layer. *Earth-Science Reviews*,
578 37(1-2), 89–134. [https://doi.org/10.1016/0012-8252\(94\)90026-4](https://doi.org/10.1016/0012-8252(94)90026-4)

579 Glenn, I. B., Feingold, G., Gristey, J. J., and Yamaguchi, T. (2020). Quantification of
580 the radiative effect of aerosol-cloud-interactions in shallow continental cumulus
581 clouds. *Journal of the Atmospheric Sciences*, 77, 2905–2920.
582 <https://doi.org/10.1175/JAS-D-19-0269.1>

583 Golaz, J. C., Larson, V. E., and Cotton, W. R. (2002). A PDF-based model for boundary
584 layer clouds. Part I: Method and model description. *Journal of the Atmospheric*
585 *Sciences*, 59(24), 3540–3551. [https://doi.org/10.1175/1520-](https://doi.org/10.1175/1520-0469(2002)059<3540:APBMFB>2.0.CO;2)
586 [0469\(2002\)059<3540:APBMFB>2.0.CO;2](https://doi.org/10.1175/1520-0469(2002)059<3540:APBMFB>2.0.CO;2)

587 Guo, J., Miao, Y., Zhang, Y., Liu, H., Li, Z., Zhang, W., ... Zhai, P. (2016). The
588 climatology of planetary boundary layer height in China derived from radiosonde
589 and reanalysis data. *Atmospheric Chemistry and Physics*, 16(20), 13,309–13,319.
590 <https://doi.org/10.5194/acp-16-13309-2016>

591 Hageli, P., Steyn, D. G., and Strawbridge, K. B. (2000). Spatial and temporal variability
592 of mixed-layer depth and entrainment zone thickness. *Boundary-Layer*
593 *Meteorology*, 97, 47–71. <https://doi.org/10.1023/A:1002790424133>

594 Holdridge, D., Ritsche, M., Prell, J., and Coulter, R. (2011). Balloon-borne sounding
595 system (SONDE) handbook. <https://www.arm.gov/capabilities/instruments/sonde>

596 Holzworth, G. C., (1964). Estimates of mean maximum mixing depths in the contiguous
597 United States, *Mon. Weather Rev.*, 92, 235–242, [https://doi.org/10.1175/1520-](https://doi.org/10.1175/1520-0493(1964)092<0235:eommmmd>2.3.co;2)
598 [0493\(1964\)092<0235:eommmmd>2.3.co;2](https://doi.org/10.1175/1520-0493(1964)092<0235:eommmmd>2.3.co;2).

599 Jones, C., Bretherton, C., and Leon, D. (2011). Coupled vs. decoupled boundary layers

600 in VOCALS-REx. *Atmospheric Chemistry and Physics*, 11(14), 7143–7153.
601 <https://doi.org/10.5194/acp-11-7143-2011>

602 Kasahara, A. (1974). Various vertical coordinate systems used for numerical weather
603 prediction. *Monthly Weather Review*, 102(7), 509–522.
604 [https://doi.org/10.1175/1520-0493\(1974\)102<0509:VVCSUF>2.0.CO;2](https://doi.org/10.1175/1520-0493(1974)102<0509:VVCSUF>2.0.CO;2)

605 Lewis, J. R., Welton, E. J., Molod, A. M., and Joseph, E. (2013). Improved boundary
606 layer depth retrievals from MPLNET. *Journal of Geophysical Research:*
607 *Atmospheres*, 118(17), 9870–9879. <https://doi.org/10.1002/jgrd.50570>

608 Lim, K.S.S., Riihimaki, L.D., Shi, Y., Flynn, D., Kleiss, J.M., Berg, L.K., Gustafson,
609 W.I., Zhang, Y. and Johnson, K.L. (2019). Long-term retrievals of cloud type and
610 fair-weather shallow cumulus events at the ARM SGP site. *Journal of Atmospheric*
611 *and Oceanic Technology*, 36(10), pp.2031-2043.

612 Liu, S. Y., and Liang, X. Z. (2010). Observed diurnal cycle climatology of planetary
613 boundary layer height. *Journal of Climate*, 23, 5790–5809.
614 <https://doi.org/10.1175/2010JCLI3552.1>

615 Lock, A. P., Brown, A. R., Bush, M. R., Martin, G. M., & Smith, R. N. B. (2000). A
616 new boundary layer mixing scheme. Part I: Scheme description and single-column
617 model tests. *Monthly weather review*, 128(9), 3187-3199.

618 Nicholls, S. (1984). The dynamics of stratocumulus: aircraft observations and
619 comparisons with a mixed layer model. *Quarterly Journal of the Royal*
620 *Meteorological Society*, 110(466), 783–820.

621 <https://doi.org/10.1002/qj.49711046603>

622 Ott, L. E., Bacmeister, J., Pawson, S., Pickering, K., Stenchikov, G., Suarez, M., ... and
623 Xueref-Remy, I. (2009). Analysis of convective transport and parameter sensitivity
624 in a single column version of the Goddard earth observation system, version 5,
625 general circulation model. *Journal of the Atmospheric Sciences*, 66(3), 627-646.

626 Platt, C. M., Young, S. A., Carswell, A. I., Pal, S. R., McCormick, M. P., Winker, D.
627 M., ... and Wooldridge, C. (1994). The Experimental Cloud Lidar Pilot Study
628 (ECLIPS) for cloud-radiation research. *Bulletin of the American Meteorological*
629 *Society*, 75, 1635–1654. [https://doi.org/10.1175/1520-](https://doi.org/10.1175/1520-0477(1994)075<1635:TECLPS>2.0.CO;2)
630 [0477\(1994\)075<1635:TECLPS>2.0.CO;2](https://doi.org/10.1175/1520-0477(1994)075<1635:TECLPS>2.0.CO;2)

631 Revercomb, H.E., Turner, D.D., Tobin, D.C., Knuteson, R.O., Feltz, W.F., Barnard, J.,
632 Bösenberg, J., Clough, S., Cook, D., Ferrare, R. and Goldsmith, J., 2003. The ARM
633 program's water vapor intensive observation periods: Overview, initial
634 accomplishments, and future challenges. *Bulletin of the American Meteorological*
635 *Society*, 84(2), pp.217-236.

636 Romps, D. M. (2017). Exact expression for the lifting condensation level. *Journal of*
637 *the Atmospheric Sciences*, 74(12), 3891–3900. [https://doi.org/10.1175/JAS-D-17-](https://doi.org/10.1175/JAS-D-17-0102.1)
638 [0102.1](https://doi.org/10.1175/JAS-D-17-0102.1)

639 Santanello Jr., J. A., Dirmeyer, P. A., Ferguson, C. R., Findell, K. L., Tawfik, A. B.,
640 Berg, A., ... and Roundy, J. (2018). Land–atmosphere interactions: the LoCo
641 perspective. *Bulletin of the American Meteorological Society*, 99(6), 1253–1272.

642 <https://doi.org/10.1175/BAMS-D-17-0001.1>

643 Sawyer, V., and Li, Z. Q. (2013). Detection, variations and intercomparison of the
644 planetary boundary layer depth from radiosonde, lidar and infrared spectrometer.
645 *Atmospheric Environment*, 79, 518–528.
646 <https://doi.org/10.1016/j.atmosenv.2013.07.019>

647 Seidel, D. J., Ao, C. O., and Li, K. (2010). Estimating climatological planetary boundary layer
648 heights from radiosonde observations: Comparison of methods and uncertainty analysis.
649 *Journal of Geophysical Research: Atmospheres*, 115(D16).

650 Silber, I., J. Verlinde, E. W. Eloranta, C. J. Flynn, and D. M. Flynn (2018), Polar liquid
651 cloud base detection algorithms for high spectral resolution or micropulse lidar data,
652 *J. Geophys. Res.: Atmos.*, doi: 10.1029/2017JD027840.

653 Storer, R.L., Griffin, B.M., Höft, J., Weber, J.K., Raut, E., Larson, V.E., Wang, M. and
654 Rasch, P.J. (2015). Parameterizing deep convection using the assumed probability
655 density function method. *Geoscientific Model Development*, 8(1), pp.1-19.

656 Stull, R. B. (1988). *An Introduction to Boundary Layer Meteorology*. Dordrecht:
657 Springer Netherlands.

658 Su, T., Li, J., Li, C. C., Xiang, P. Z., Lau, A. K. H., Guo, J. P., ... and Miao, Y. C. (2017b).
659 An intercomparison of long-term planetary boundary layer heights retrieved from
660 CALIPSO, ground-based lidar, and radiosonde measurements over Hong Kong.
661 *Journal of Geophysical Research: Atmospheres*, 122, 3929–3943.
662 <https://doi.org/10.1002/2016JD025937>

663 Su, T., Li, J., Li, J., Li, C., Chu, Y., Zhao, Y., ... Wang, L. (2017a). The evolution of
664 springtime water vapor over Beijing observed by a high dynamic Raman lidar
665 system: case studies. *IEEE Journal of Selected Topics in Applied Earth
666 Observations and Remote Sensing*, 10(5), 1715–1726.
667 <https://doi.org/10.1109/JSTARS.2017.2653811>

668 Su, T., Li, Z., and Kahn, R. (2018). Relationships between the planetary boundary layer
669 height and surface pollutants derived from lidar observations over China: regional
670 pattern and influencing factors. *Atmospheric Chemistry and Physics*, 18(21),
671 15,921–15,935. <https://doi.org/10.5194/acp-18-15921-2018>

672 Su, T., Li, Z., and Kahn, R. (2020). A new method to retrieve the diurnal variability of
673 planetary boundary layer height from lidar under different thermodynamic stability
674 conditions. *Remote Sensing of Environment*, 237, 111519.
675 <https://doi.org/10.1016/j.rse.2019.111519>

676 Teixeira, J., and Hogan, T. F. (2002). Boundary layer clouds in a global atmospheric
677 model: simple cloud cover parameterizations. *Journal of Climate*, 15(11), 1261–
678 1276. [https://doi.org/10.1175/1520-0442\(2002\)015<1261:BLCIAG>2.0.CO;2](https://doi.org/10.1175/1520-0442(2002)015<1261:BLCIAG>2.0.CO;2)

679 M. (1996). Evaluation and model impacts of alternative boundary-layer height
680 formulations. *Boundary-Layer Meteorology*, 81(3-4), 245–269.
681 <https://doi.org/10.1007/BF02430331>

682

683 Wallace, J. M., and Hobbs, P. V. (2006). *Atmospheric Science: an Introductory Survey*.

684 Amsterdam, Boston: Elsevier Academic Press.

685 Warren, G., Hahn, C. J., London, J., Chervin, M., and Jenne, R. L. (1986). Global
686 distribution of total cloud cover and cloud type amounts over land. (Rep. DOE/ER-
687 0406). Washington, DC: U.S. DOE Office of Energy Research.

688 Wei, J., Huang, W., Li, Z., Sun, L., Zhu, X., Yuan, Q., Liu, L. and Cribb, M., 2020.
689 Cloud detection for Landsat imagery by combining the random forest and
690 superpixels extracted via energy-driven sampling segmentation approaches.
691 *Remote Sensing of Environment*, 248, p.112005.

692 Welton, E. J., Campbell, J. R., Spinhirne, J. D., and Scott III, V. S. (2001). Global
693 monitoring of clouds and aerosols using a network of micropulse lidar systems. In
694 *Lidar Remote Sensing for Industry and Environment Monitoring* (Vol. 4153, 151–
695 158). International Society for Optics and Photonics.

696 Wu, X., Grabowski, W. W, and Moncrieff, M. W. (1998). Long-term behavior of cloud
697 systems in TOGA COARE and their interactions with radiative and surface
698 processes. Part I: Two-dimensional modeling study. *Journal of the Atmospheric*
699 *Sciences*, 55(17), 2693–2714. [https://doi.org/10.1175/1520-
700 0469\(1998\)055<2693:LTBOCS>2.0.CO;2](https://doi.org/10.1175/1520-0469(1998)055<2693:LTBOCS>2.0.CO;2)

701 Yang, D., Li, C., Lau, A. K. H., and Li, Y. (2013). Long-term measurement of daytime
702 atmospheric mixing layer height over Hong Kong. *Journal of Geophysical*
703 *Research: Atmospheres*, 118(5), 2422–2433. <https://doi.org/10.1002/jgrd.50251>

704 Yang, T., Wang, Z., Zhang, W., Gbaguidi, A., Sugimoto, N., Wang, X., Matsui, I. and

705 Sun, Y., 2017. Boundary layer height determination from lidar for improving air
706 pollution episode modeling: development of new algorithm and evaluation.
707 *Atmospheric Chemistry and Physics*, 17(10), p.6215.

708 Zhao, C., Wang, Y., Wang, Q., Li, Z., Wang, Z., and Liu, D. (2014). A new cloud and
709 aerosol layer detection method based on micropulse lidar measurements. *Journal*
710 *of Geophysical Research: Atmospheres*, 119(11), 6788–6802.
711 <https://doi.org/10.1002/2014JD021760>

712 Zheng, Y., and Li, Z. (2019). Episodes of warm-air advection causing cloud-surface
713 decoupling during the MARCUS. *Journal of Geophysical Research: Atmospheres*,
714 124(22). <https://doi.org/10.1029/2019JD030835>

715 Zheng, Y., and Rosenfeld, D. (2015). Linear relation between convective cloud base
716 height and updrafts and application to satellite retrievals. *Geophysical Research*
717 *Letters*, 42(15), 6485–6491. <https://doi.org/10.1002/2015GL064809>

718 Zheng, Y., Rosenfeld, D., and Li, Z. (2018). Estimating the decoupling degree of
719 subtropical marine stratocumulus decks from satellite. *Geophysical Research*
720 *Letters*, 45. <https://doi.org/10.1029/2018GL078382>

721 Zheng, Y., Sakradzija, M., Lee, S.-S., and Li, Z. (2020). Theoretical understanding of
722 the linear relationship between convective updrafts and cloud-base height for
723 shallow cumulus clouds. Part II: Continental conditions. *Journal of the*
724 *Atmospheric Sciences*, 77, 1313–1328. <https://doi.org/10.1175/JAS-D-19-0301.1>

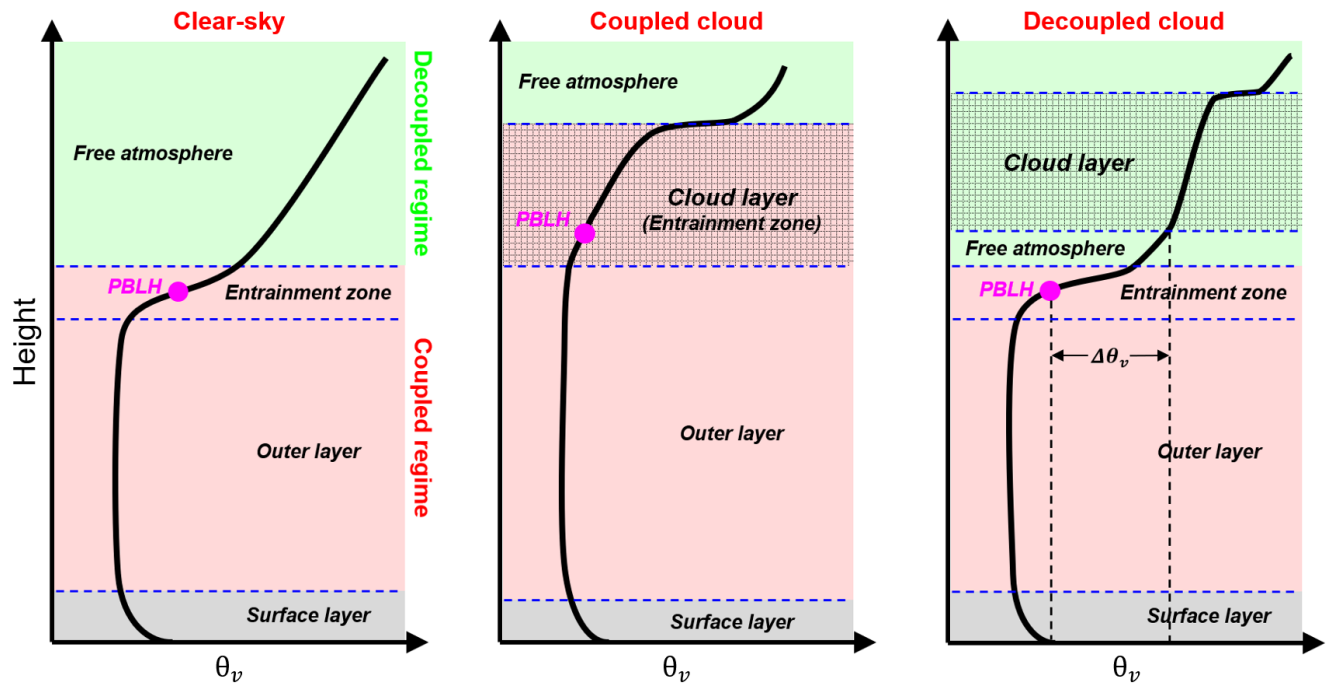
725

726 **Tables**

727 **Table 1.** List of parameters in the flow chart of DTDS (Figure 4). These parameters are
 728 related with three factors, including LCL, PBLH, CBH. The sensitivity of selection of
 729 these parameters is presented. The detailed impacts of variations in these parameters on
 730 the retrievals of cloud coupling and PBLH are presented in Figure 6 and Figure 7,
 731 respectively.

732

	Unit	Related factors	Value	Sensitivity (coupled states)	Sensitivity⁷³³ (PBLH)
A₁	km	LCL / PBLH	0.7	Low	Low
A₂	km	PBLH	0.2	High	Low
A₃	km	LCL	0.15	Low	Low
A₄	dimensionless	CBH	1.35	Low	Low
A₅	dimensionless	CBH	1.1	Low	High

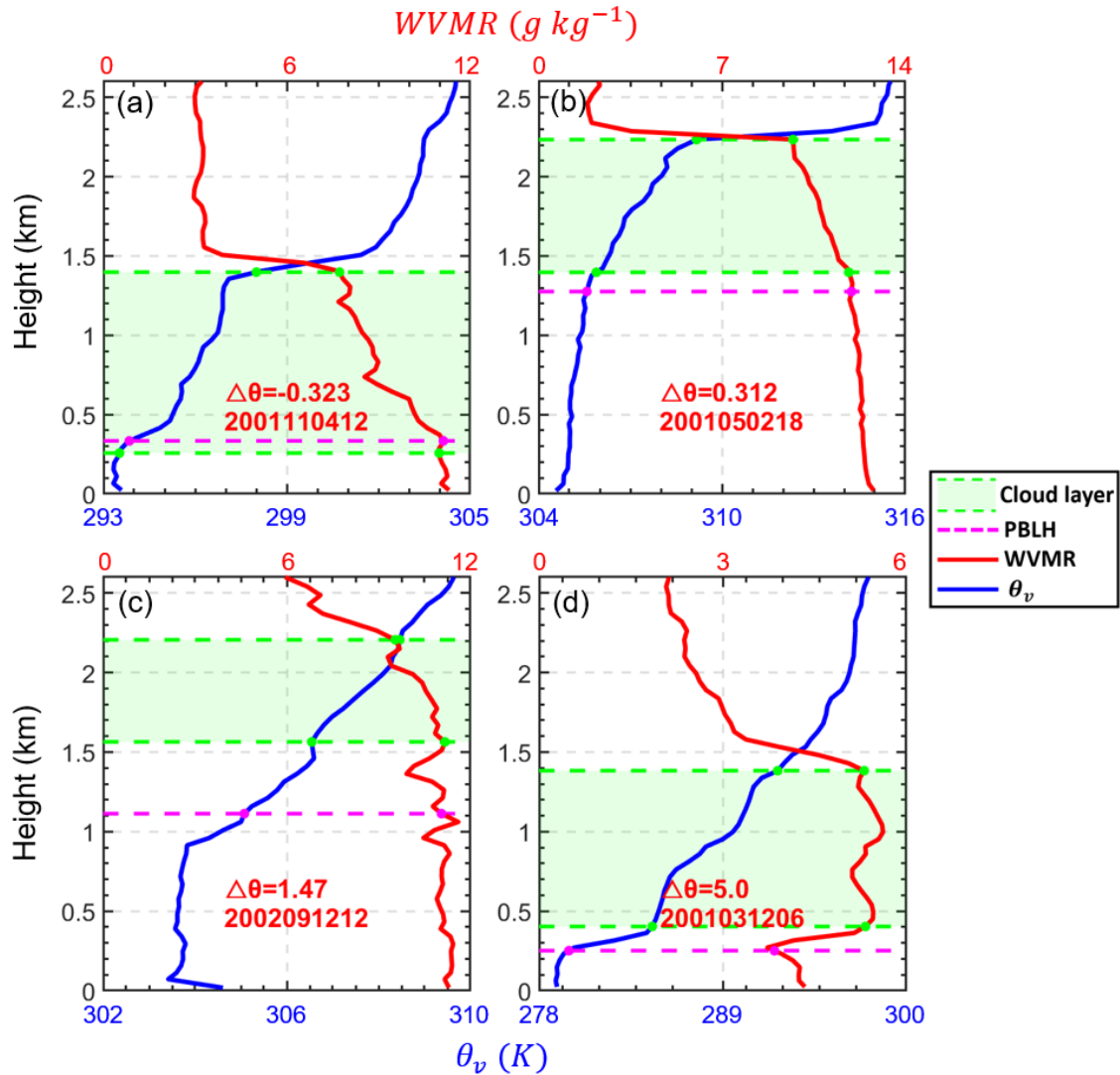


735

736 **Figure 1.** Idealized vertical profiles of virtual potential temperature (θ_v) under the clear-
 737 sky, coupled cloud, and decoupled cloud over land. The surface layer, outer layer
 738 entrainment zone, and free atmosphere are divided by the blue dash lines. The cloudy
 739 layer is marked as the shaded area, and PBLH is marked as the pink point. Red and
 740 green zones indicate the coupled and decoupled regime, respectively. Elements (e.g.,
 741 turbulence, heat fluxes, cloud) in the coupled regime are directly affected by the PBL
 742 processes, while these elements are not directly affected by the PBL processes in the
 743 decoupled regime. For the coupled cases, the cloud base is below the capping
 744 of entrainment zone. For the decoupled cases, the cloud base is above the capping
 745 inversion.

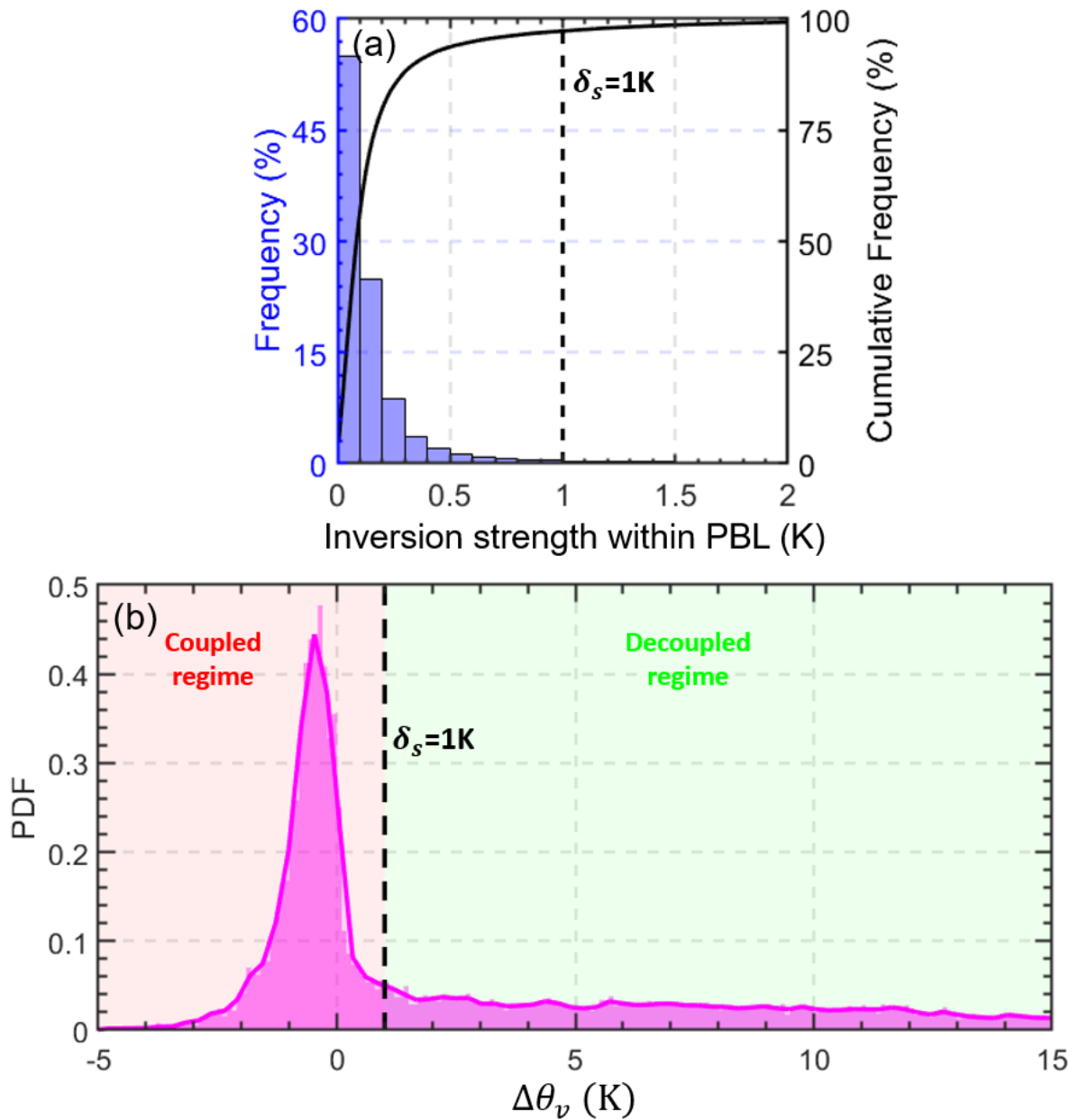
746

747



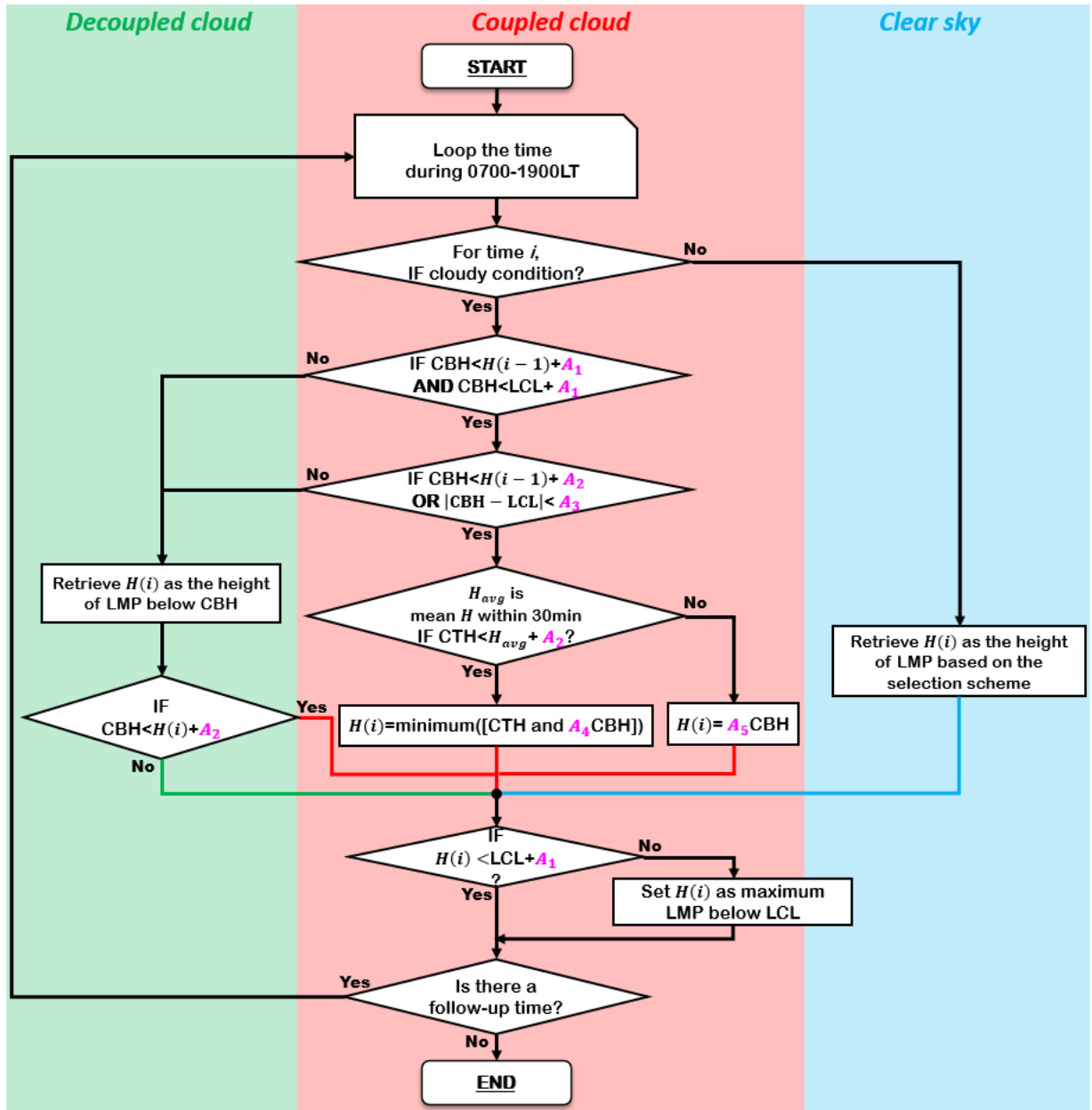
748

749 **Figure 2.** Virtual potential temperature (θ_v , red lines) and water vapor mixing ratio
 750 (WVMR, blue lines) profiles from radiosonde (RS) over the Southern Great Plains site
 751 for different cases. The differences in virtual potential temperature between the cloud
 752 base and the planetary boundary layer (PBL) top are expressed as $\Delta\theta_v$ ($\theta_v^{\text{CBH}} -$
 753 θ_v^{PBLH}). The time of each radiosonde launch is marked in each panel as
 754 “YYYYMMDDHH”, where YYYY, MM, DD, and HH indicates the year, month, day,
 755 and local time, respectively. Green regions are cloud layers, and green dashed lines
 756 indicate their boundaries. The cloud layer is obtained from the CLDTYPE/ARSCL data.
 757 PBLHs is derived from RS data, and is marked as dashed pink lines.



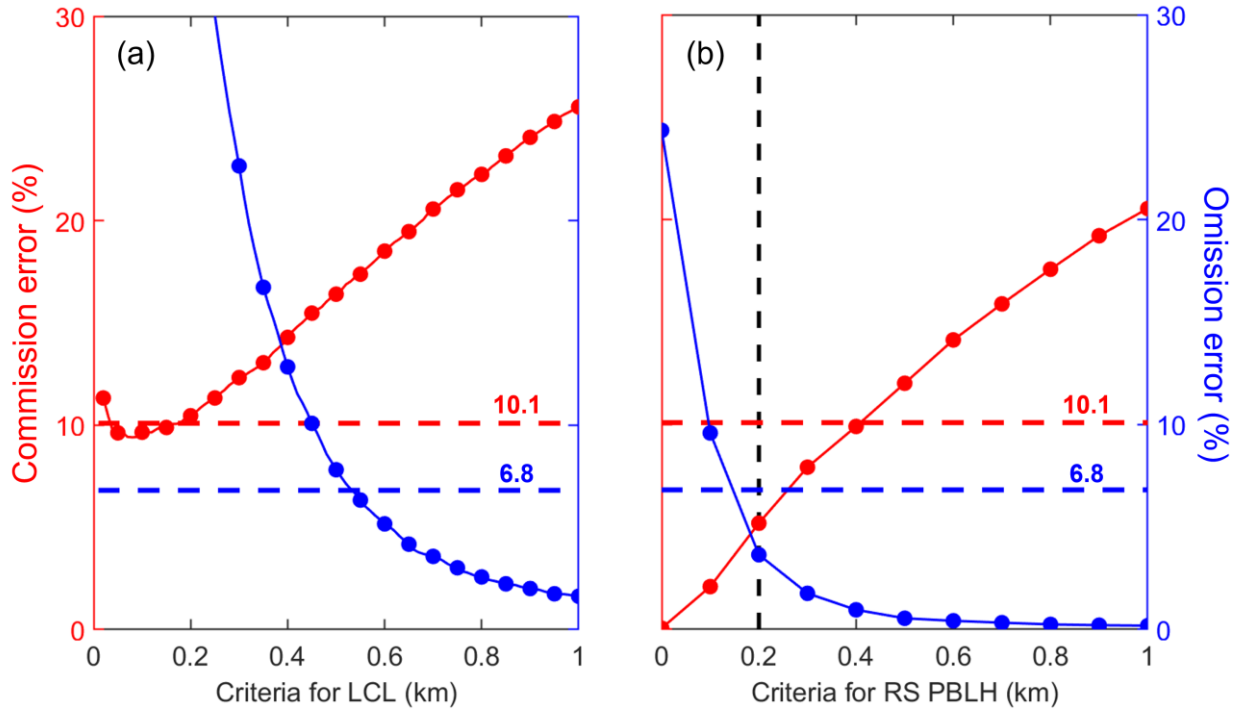
758

759 **Figure 3.** (a) Blue bars represent the inversion strength of θ_v within the PBL. The
 760 inversion strength is derived from the radiosonde during daytime (0800-1900LT). The
 761 inversions near surface or across PBL top are excluded. The black solid line represents
 762 cumulative frequency. (b) Pink area represents the probability density function (PDF)
 763 of the differences in the virtual potential temperature between cloud-base height (CBH)
 764 and PBLH ($\Delta\theta_v = \theta_v^{\text{CBH}} - \theta_v^{\text{PBLH}}$). By using a threshold of δ_s (1 K), coupled and
 765 decoupled regimes are classified.



766

767 **Figure 4.** The flow chart of the updated DTDS algorithm. In this diagram, $H(i)$ is the
 768 retrieved planetary boundary layer height (PBLH) at time i . CBH and CTH represent
 769 the base and top heights, respectively, of the lowest cloud at time i . The PBLH part for
 770 selecting the suitable local maximum position (LMP) follows Su et al. (2020), and a
 771 detailed scheme for identifying a coupled cloud is added to the DTDS algorithm. LCL
 772 stands for lifted condensation level. Five empirical parameters (A_1, A_2, A_3, A_4, A_5) are
 773 set as 0.7, 0.2, 0.15, 1.35, 1.1, respectively.



774

775 **Figure 5.** Commission errors and omission errors of coupled cloud identifications (a)

776 for different criteria for the lifted condensation level (LCL) and (b) for different criteria

777 for the planetary boundary layer height (PBLH). “Criteria for LCL” means coupled

778 clouds are identified if $|CBH - LCL| < \text{Criteria for LCL}$. Similarly, “Criteria for RS

779 PBLH” means coupled clouds are identified if $CBH - RS \text{ PBLH} < \text{Criteria for RS}$

780 PBLH. The red and blue dashed lines indicate the commission and omission errors,

781 respectively, for the DTDS algorithm. CBH stands for cloud-base height, and RS stands

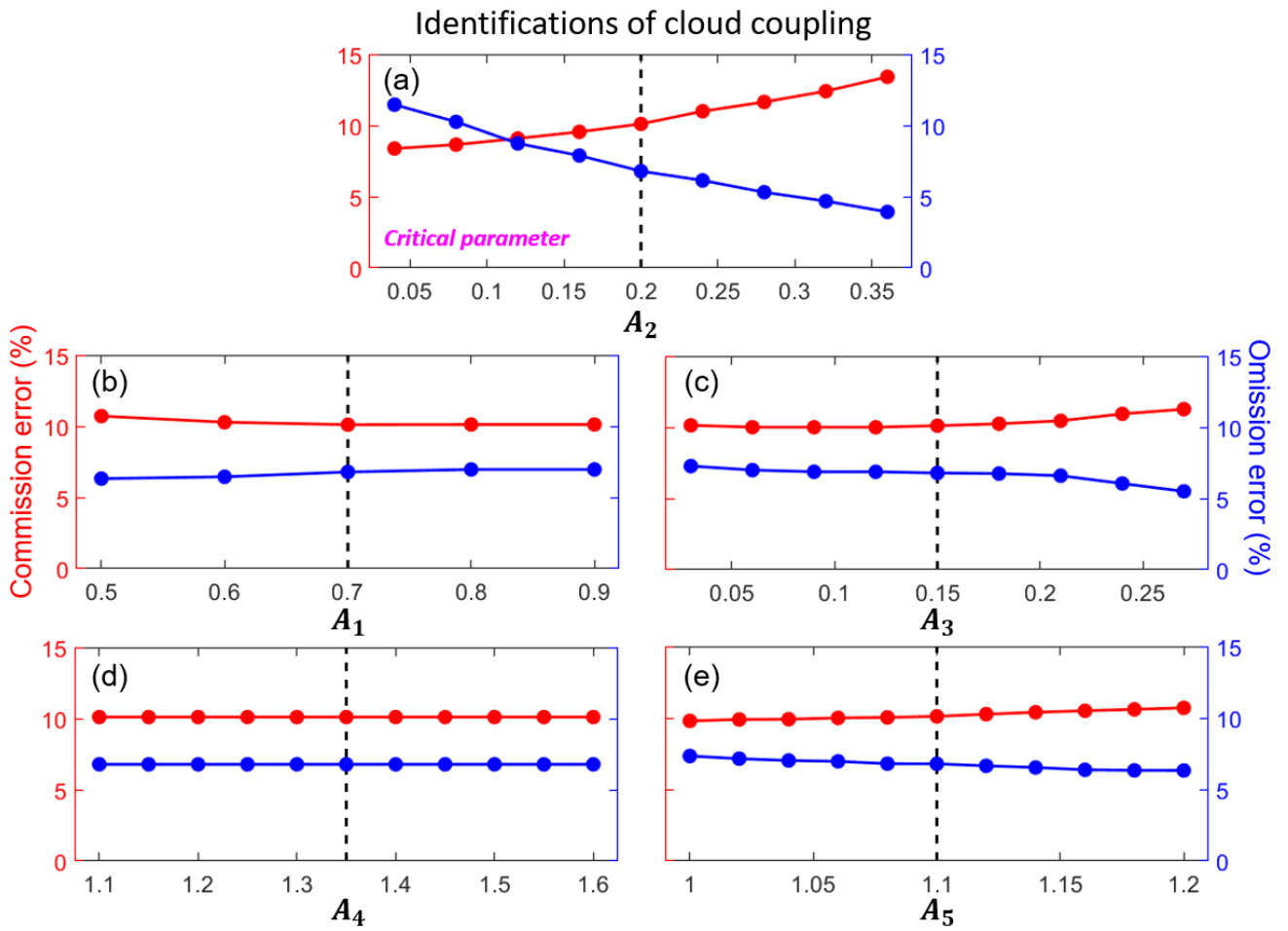
782 for radiosonde. By using ~ 7500 RS profiles, the cloud coupling state derived from the

783 virtual potential temperature method (Section 3.1) is considered as the ground truth for

784 evaluation.

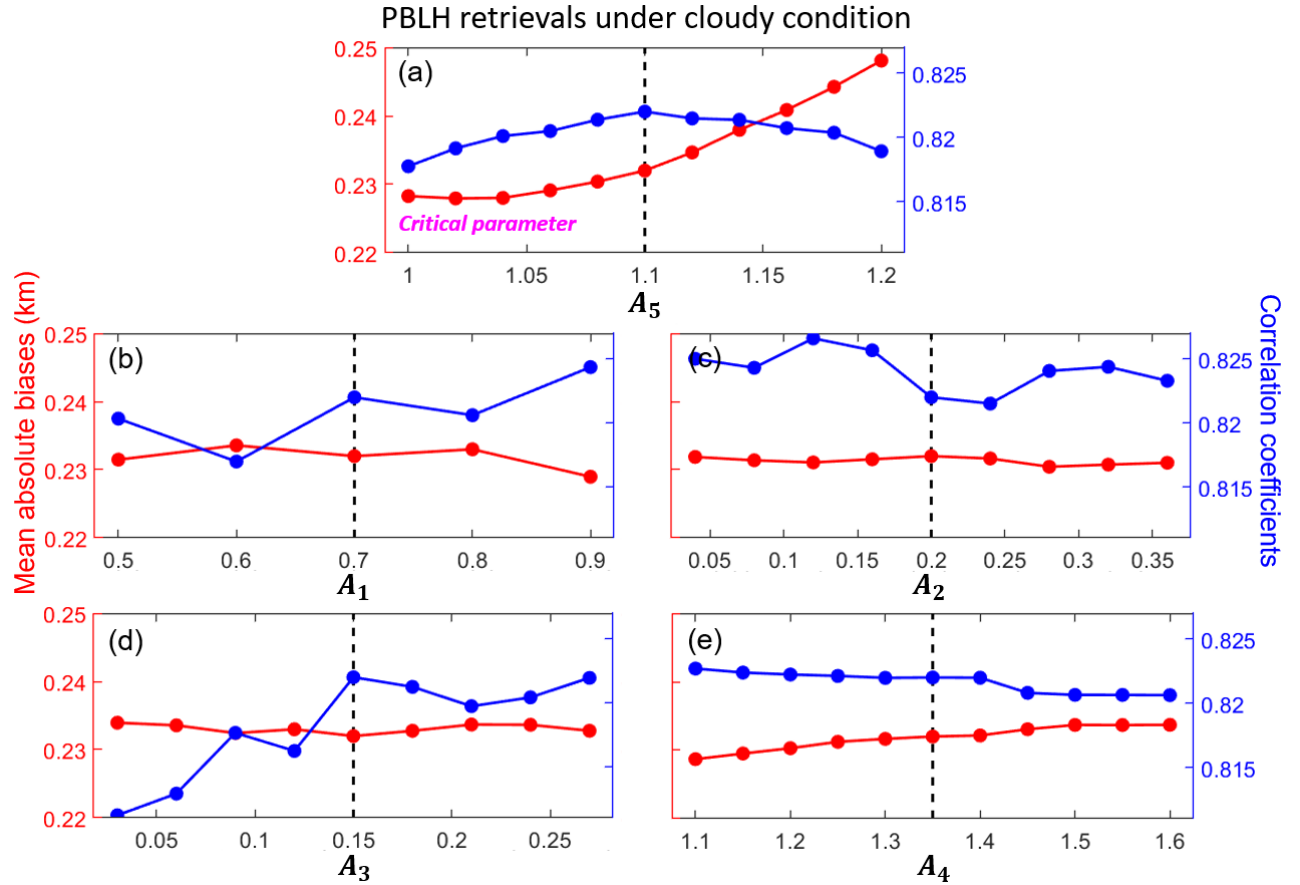
785

786



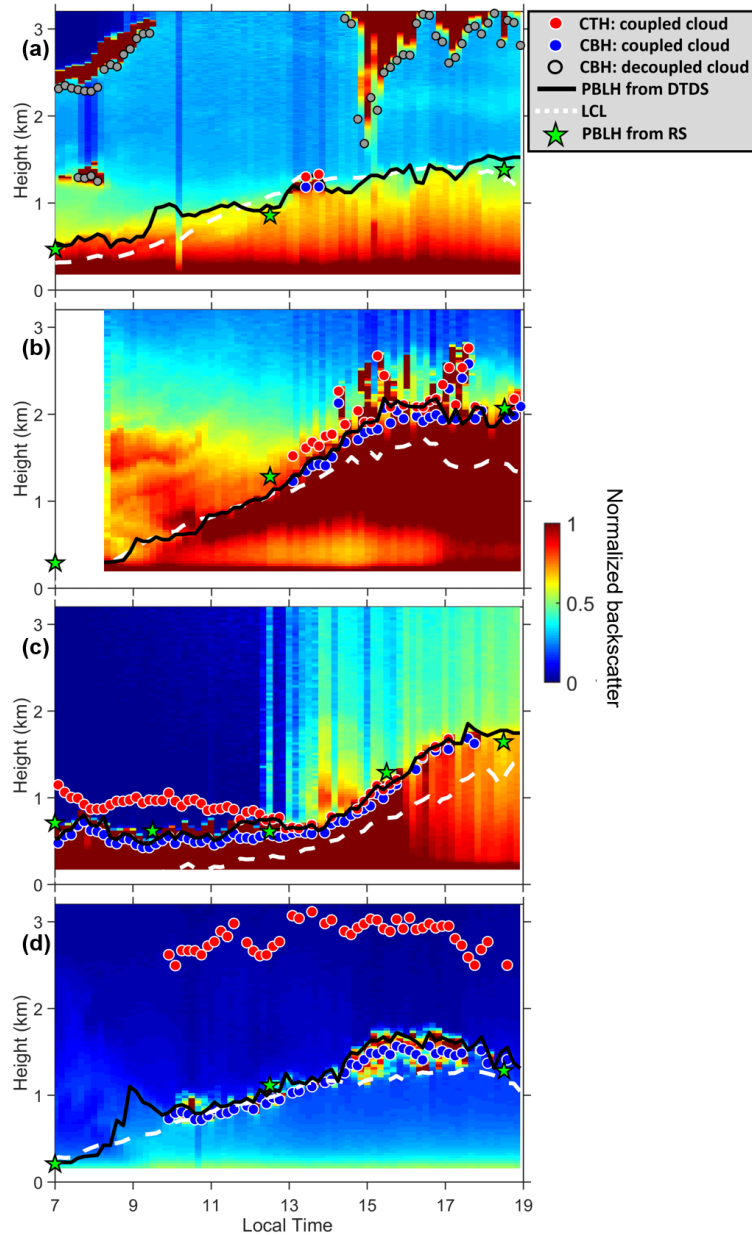
787

788 **Figure 6.** Commission errors (red line) and omission errors (blue line) of coupled cloud
 789 identifications for selecting different values of empirical parameters (A_1, A_2, A_3, A_4, A_5)
 790 in the DTDS algorithm. Black dash lines indicate the default values. For each test, one
 791 parameter is variable, while other parameters are set as default values. For
 792 identifications of cloud coupling, A_2 is the critical parameter.



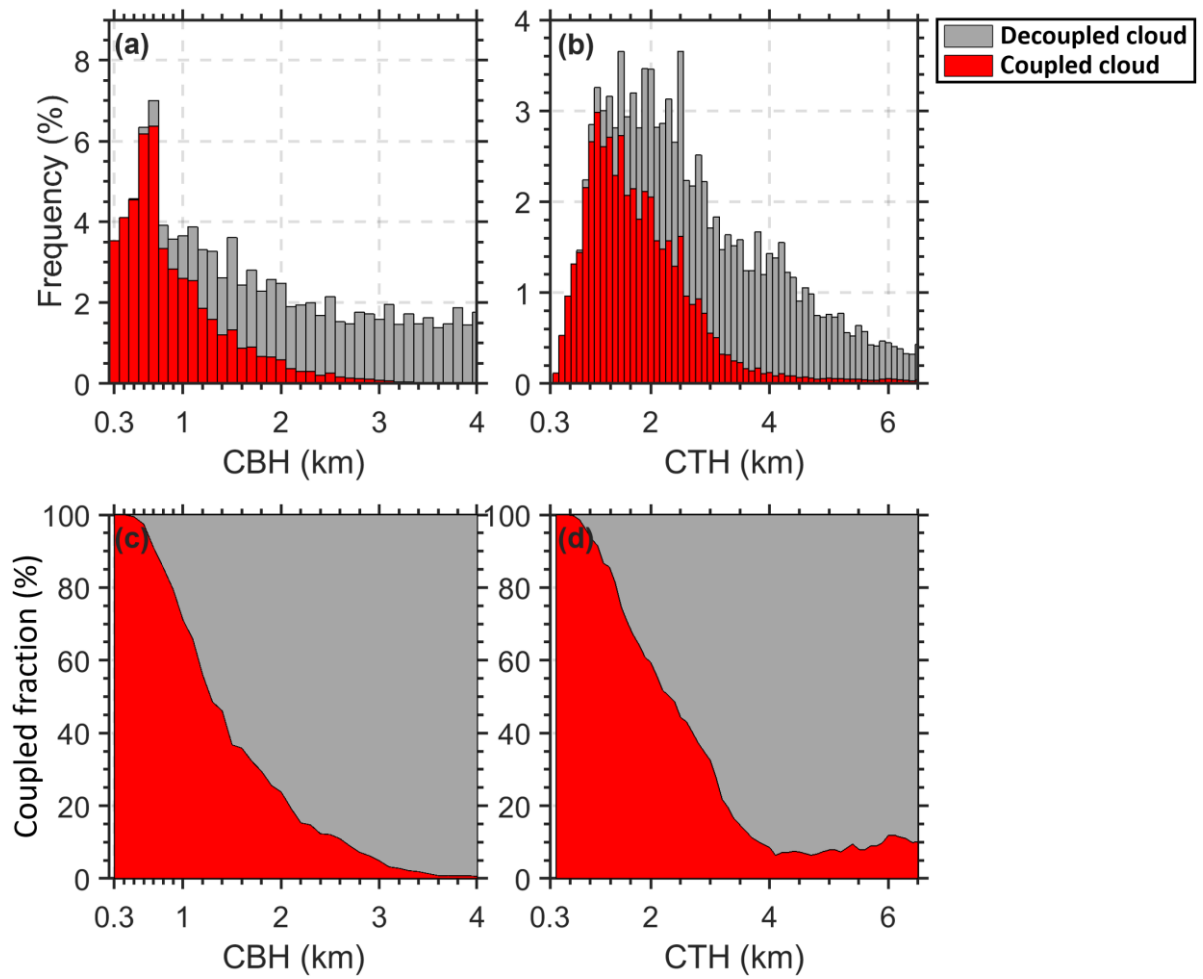
793

794 **Figure 7.** Red lines indicate the mean absolute biases between PBLH derived from lidar
 795 and radiosonde for selecting different values of empirical parameters (A_1, A_2, A_3, A_4, A_5)
 796 in the DTDS algorithm. Here, we only analyze the low cloud cases. Blue lines indicate
 797 the corresponding correlation coefficients between PBLH derived from lidar and
 798 radiosonde. Black dash lines indicate the default values. For each test, one parameter is
 799 variable, while other parameters are set as default values. For PBLH retrievals under
 800 cloudy conditions, A_5 is the critical parameter.



801

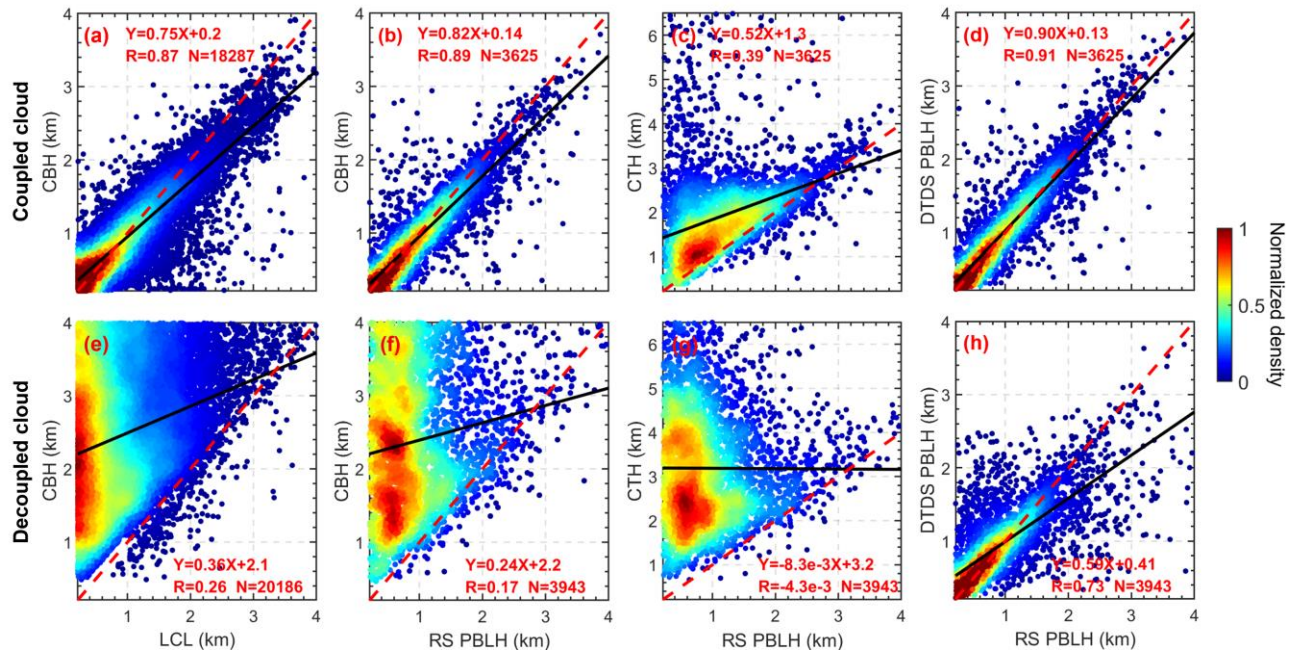
802 **Figure 8.** Daily backscatter profiles: (a) short-lived coupled cloud, (b) developed
 803 coupled cloud, (c) daylong coupled cloud, and (d) active coupled cloud. Backscatter is
 804 normalized to a range of 0–1 in arbitrary units. Red dots and blue dots indicate cloud-
 805 top heights (CTHs) and cloud-base heights (CBHs) of coupled clouds. Grey dots mark
 806 CBHs for decoupled clouds. Black lines and green stars mark the planetary boundary
 807 layer height (PBLH) retrieved from the DTDS algorithm and from radiosonde (RS)
 808 soundings, respectively. White dashed lines represent lifted condensation levels (LCLs).



809

810 **Figure 9.** The height-dependent occurrence frequencies of (a) the cloud-base height
 811 (CBH) and (b) the cloud-top height (CTH) for coupled clouds (red bars) and decoupled
 812 clouds (grey bars). The relative occurrence frequencies of (c) the CBH and (d) the CTH
 813 for coupled clouds (red area) and decoupled clouds (grey area).

814



815

816 **Figure 10.** The relationships between (a) LCL and CBH, (b) CBH and RS-derived
 817 PBLH, (c) CTH and RS-derived PBLH for coupled clouds, and (d) DTDS-derived
 818 PBLH and RS-derived PBLH. Panels (e-h) are similar to panels (a-d) but for decoupled
 819 clouds. Black lines represent the linear regressions. The linear fitting functions,
 820 correlation coefficients (R), and sampling numbers (N) are given in each panel.